Supporting Information

Lead halide coordination competition at buried interface for low V_{OC}-deficits in wide bandgap perovskite solar cells

Hongsen Cui, Lishuai Huang, Shun Zhou, Chen Wang, Xuzhi Hu, Hongling Guan, Shuxin Wang, Wenlong Shao, Dexin Pu, Kailian Dong, Jin Zhou, Peng Jia, Weizhong Wang*, Chen Tao*, Weijun Ke*, and Guojia Fang*

Methods

Materials

2PACz ([2-(9H-carbazol9-yl)ethyl]phosphonic acid), and Me-4PACz ([4-(3,6dimethyl-9H-carbazol-9-yl)butyl]phosphonic acid) were purchased from TCI. $Pb(SCN)_2$ (lead thiocyanate) and CsI (cesium iodide) were purchased from Sigma-Aldrich. PbI_2 (lead iodide), $PbBr_2$ (lead bromide) and FAI (formamidinium iodide) was purchased from Advanced Election Technology Co.,Ltd. C60 was purchased from Xi'an polymer light technology. N, N-dimethyl formamide (DMF), isopropanol (IPA), chlorobenzene (CB), and dmethyl sulfoxide (DMSO) were acquired from Sigma-Aldrich. PEDOT:PSS (Clevios PVP Al4083) was purchased from Heraeus.

Single Junction Perovskite Device Fabrication

The precursor solution for perovskite film deposition was prepared by mixing FAI, CsI, $PbBr_2$, and PbI_2 in a mixture of DMF and DMSO at a concentration of 1.2 M. The molar ratios of FA^+/Cs^+ and I^-/Br^- were maintained at 8:2 and 6:4, respectively. Additionally, a 1 mol% concentration of $Pb(SCN)_2$ was included, which was found to improve device performance.

The precursor solution was stirred at 60 °C for 2 hours and then cooled to room temperature. The ITO glass substrate was cleaned by sequentially washing it with detergent, deionized water, acetone, and ethanol. The substrate was dried with N_2 and further cleaned with ultraviolet ozone for 15 minutes.

For the control group devices, a solution of 2PACz in absolute ethanol (0.3 mg ml^{-1}) was spin-coated on the clean ITO substrates as the hole selective layer. The spin-coating was performed at 3,000 r.p.m. for 30 seconds, followed by annealing at 100 °C for 10 minutes. For the target group devices, after spin-coating the 2PACz solution, another solution of Me-4PACz in absolute ethanol (0.3 mg ml^{-1}) was spin-coated on the substrates at 3,000 r.p.m. for 30 seconds, followed by annealing at 100 °C for 10 minutes. The perovskite films were deposited on the substrates using a two-step spin-

coating procedure. The first step involved spinning at 2,000 rpm for 10 seconds with an acceleration of 200 rpm s^{-1}. The second step involved spinning at 6,000 rpm for 40 seconds with a ramp-up of 2,000 rpm s^{-1}. During the second spin-coating step, 400 µl of diethyl ether was dropped onto the spinning substrate at 30 seconds before the end of the procedure. The substrates were then transferred to a hotplate and heated with a two-step procedure: 60 °C for 2 minutes, followed by 100 °C for 10 minutes. After cooling to room temperature, a solution of PDADI in IPA (isopropyl alcohol) (2 mg ml^{-1}) was dropped onto the perovskite film and spin-coated at 4,000 r.p.m. for 30 seconds. The substrate was then annealed at 100 °C for 10 minutes.

Subsequently, the electron transport layers (ETLs) C60 (20 nm), BCP (7 nm), and the metal electrode (Cu, 120 nm) were evaporated onto the substrate using a high-vacuum thermal evaporator (Wuhan PDVacuum Technologies Co.,Ltd). The active area of the devices was defined using a shadow mask.

Fabrication of semi-transparent WBG PSCs

For the semitransparent cells, a 20 nm layer of atomic layer deposition (ALD) SnO$_X$ was utilized instead of BCP (bathocuproine). The precursors used for ALD SnO$_X$ deposition were tetrakis(dimethylamino) tin(IV) and deionized water. Subsequently, a 100 nm layer of indium tin oxide (ITO) was sputtered onto the substrate. The sputtering process was performed at a power of 100 W under an Ar$_2$ pressure of 2 m Torr. The active area of the devices was defined as 0.070225 cm^2 and was determined by the overlapping region between the back electrode and the patterned ITO substrate.

Fabrication of narrow-bandgap (NBG) PSCs

The cleaning of ITO substrates is the same as the above process in WBG PSCs. Next, PEDOT: PSS solutions were spin-coated on the substrates at 5000 rpm for 30 s and annealed at 140°C for 30 min. After annealing, the substrates were immediately transferred into an N$_2$-filled glovebox. The perovskite precursors after filtering were directly deposited on the substrates by a one-step spin-coating method at 1000 rpm for 10 s and 4000 rpm for 40 s. 400 µL of CB was dropped on the films at the 20th

second before the end of spin-coating. The substrates with perovskite films were annealed at 100°C for 10 min. In the following, the post-treatment solutions were spin-coated onto the perovskite films at 4000 rpm for 30 s, and the films were annealed at 100 °C for 7 min. Finally, C60 (20 nm), BCP (7 nm), and Cu (80 nm) were thermally evaporated under a high vacuum chamber (1×10^{-4} Pa) to complete the devices.

Fabrication of 2-T tandem PSCs

For the 2-T tandem cells, a 20 nm layer of atomic layer deposition (ALD) SnO_X was utilized instead of BCP (bathocuproine). A thin layer of 1 nm Au was deposited by thermal evaporation under a high vacuum chamber (1×10^{-4} Pa). Next, PEDOT: PSS solutions were spin-coated on the substrates at 5000 rpm for 30 s and annealed at 140°C for 30 min. After annealing, the substrates were immediately transferred into an N_2-filled glovebox for the fabrication of the NBG subcell as mentioned above.

Characterization and analysis

Film characterization

Films (hole selective layer and perovskite layer) were prepared on ITO glass substrate, 2PACz coated ITO glass / (denoted as "control") and 2PACz/Me-4PACz coated ITO glass (denoted as "target") for characterization and comparison studies. PLQY measurements were characterized by a system with an integrating sphere and an excitation wavelength of 365 nm. The fixed light intensity of 100 mW $cm^{-2}$was used for the PLQY measurements. The contact angle of perovskite precursor on different substrates (Glass/ITO/2PACz or Glass/ITO/2PACz/Me-4PACz) was determined using a SL200KB dynamic contact angle analyzer. The perovskite bottom interface was characterized with XPS, SEM, KPFM, PL Mapping and the thin film preparation procedure was shown in Figure S6. XPS measurements were conducted with a monochromatic Al-Kα x-ray source by an XPS/UPS system (Thermo Scientific, ESCLAB 250Xi). XPS spectra were fitted using a Thermo Advantage software. Preceding the fitting process, energy levels were meticulously calibrated, with the

reference C1s level set at 284.6 eV. The morphology of the films was observed using scanning electron microscopy (SEM) with a Zeiss SIGMA microscope operating at an accelerating voltage of 5 kV. AFM and KPFM images were observed by a Bruker Dimension Icon XR equipment in a Scanasyst-Air and Peak force KPFM Mode. PL mapping was captured by a confocal laser scanning fluorescence microscopy (CLSM) (TCS SP8, Leica). A 552 nm laser was applied as the PL excitation source to detect and collect the PL signals at 650–750 nm. The crystal structures and phases of the perovskite films deposited on different substrates (Glass/ITO/2PACz for control samples and Glass/ITO/2PACz/Me-4PACz for target samples) were characterized using an X-ray diffraction (XRD) instrument, specifically the Bruker AXS D8 Advance model with a scan speed of 5 degrees min^{-1}. UPS spectra were conducted in the Thermo Scientific Escalab 250Xi XPS/UPS system with a He I UV source at a bias voltage of -6 V. The absorption spectra of the films were measured using a Shimadzu UV-vis spectrophotometer, specifically the miniUV-1208 model. Surface roughness of the films were characterized with a Bruker Dimension Icon XR AFM. Photoluminescence (PL) spectra of the perovskite films were recorded using a HORIBA Delta Flex fluorescence spectrometer equipped with a semiconductor laser emitting at a center wavelength of 481 nm. Time-resolved photoluminescence (TRPL) measurements were performed using a time-correlated single-photon counting (TCSPC) module. The specific details are shown in the Figure S15.

Device characterization

First, primitive J-V curves were obtained using a Keithley 2400 source meter under standard AM 1.5 G illumination (100mW cm^{-2}) produced by a solar simulator (Enlitech, SS-F5-3A), and the original J_{SC} is derived from the curve. The solar simulator was calibrated to a 100mW cm^{-2} light intensity by a National Renewable Energy Laboratory-certified and KG3-filtered crystalline silicon solar cell. This sample is then placed in the EQE test system (Enli Technology Co. Ltd.), resulting in an integral J_{EQE}. The original Jsc is then calibrated by a coefficient based on the J_{EQE}

obtained by the integral, so as to match the integral J_{EQE} measured by the EQE test (error range less than 2%).

Current-voltage (*J-V*) curves and steady-state power outputs of the perovskite solar cells (PSCs) were measured under air mass 1.5 global (AM 1.5 G) conditions, with the measurements performed by Enli Technology Co. Ltd in a nitrogen atmosphere. A metal mask was used to mask the active area during the measurements, with a hole area being 0.070225 cm². The *J-V* measurements were carried out with a scan rate of 20 mV/s, covering a voltage range from 1.37 V to -0.1 V and then reversed back from -0.1 V to 1.37 V (-0.1V to 2.2V for 2-T tandem), with a dwell time of 50 ms at each voltage point. Space charge limited current (SCLC) curves of single-carrier devices were recorded using a Keithley 2400 source meter in the dark. Mott-Schottky curves with capacitance-voltage measurements were performed using a CHI760E electrochemical workstation from Shanghai Chenhua Instruments at 1 kHz. The bias voltages ranged from 1.5 V to 0 V, and an AC voltage of 20 mV was used to measure the corresponding capacitance at the different bias voltages.

Density functional theory (DFT) calculations

The magnitudes of the binding energies were calculated by the density functional theory method. All first-principle calculations were performed with the Vienna Ab-initio Simulation Package (VASP). Electron–nuclei interactions were described by the projector-augmented wave pseudopotentials. The Perdew–Burke–Ernzerhof exchange-correlation functional was investigated in all calculations. The Kohn–Sham wave functions were expanded in plane waves up to 520 eV. The models were built with a vacuum region of more than 15 Å in all the XYZ-directions. The binding energies were calculated based on the energy difference between the different models. The convergence threshold of energy in the self-consistent step was set as 10^{-5} eV with a Gaussian smearing of 0.05 eV Å^{-1}. Moreover, the force threshold of geometry optimization is 0.05 eV Å^{-1} for each dimension of all atoms in the model.

Four-terminal (4-T) tandem solar cells

In the characterization of the 4-T tandem solar cells, the power conversion efficiencies (PCEs) of the top semi-transparent wide-bandgap (WBG) perovskite solar cells (PSCs) were initially measured. Subsequently, the PCEs of the bottom narrow-bandgap (NBG) PSCs were measured, with the incident light filtered through the top semi-transparent WBG PSCs. To minimize optical losses, silicone oil was applied in the air gap between the WBG PSCs and the NBG PSCs, following a previous report.[1] The PCEs of the 4T all-perovskite tandem solar cells were calculated as the sum of the efficiencies of the top cells and bottom cells.

Supplementary Note 1: Calculation of V_{OC} nonradiative recombination loss

The relationship between the photoluminescence quantum yield (PLQY) and the quasi-Fermi level splitting (QFLS) in the perovskite film can be described by the following equation, assuming that all photoluminescence (PL) emission originates from radiative recombination of free charges:[2]

$$QFLS = QFLS_{rad} + K_B T ln(PLQY) \qquad (1)$$

In Equation (1), $QFLS_{rad}$ represents the $QFLS$ for the perovskite layer when only radiative recombination occurs. K_B is the Boltzmann constant, T is the temperature, and $-K_B T ln(PLQY)$ represents the QFLS loss due to nonradiative recombination. Additionally, the nonradiative recombination loss (ΔV_{OC}) in the V_{OC} can be calculated using the following equation:

$$\Delta V_{OC} = \frac{QFLS_{rad} - QFLS}{q} = -\frac{K_B T ln(PLQY)}{q} \qquad (2)$$
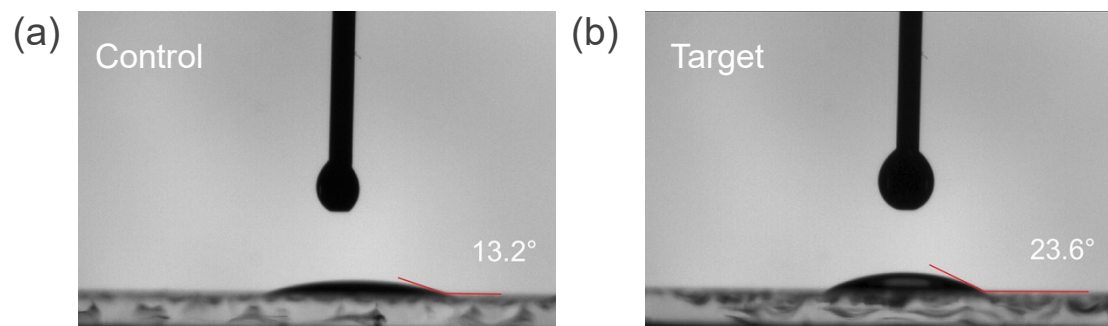
Figure S1. Contact angle measurements using perovskite solution as a test solvent. Contact angle of 2PACz (a) and 2PACz with Me-4PACz (b) on ITO substrates.
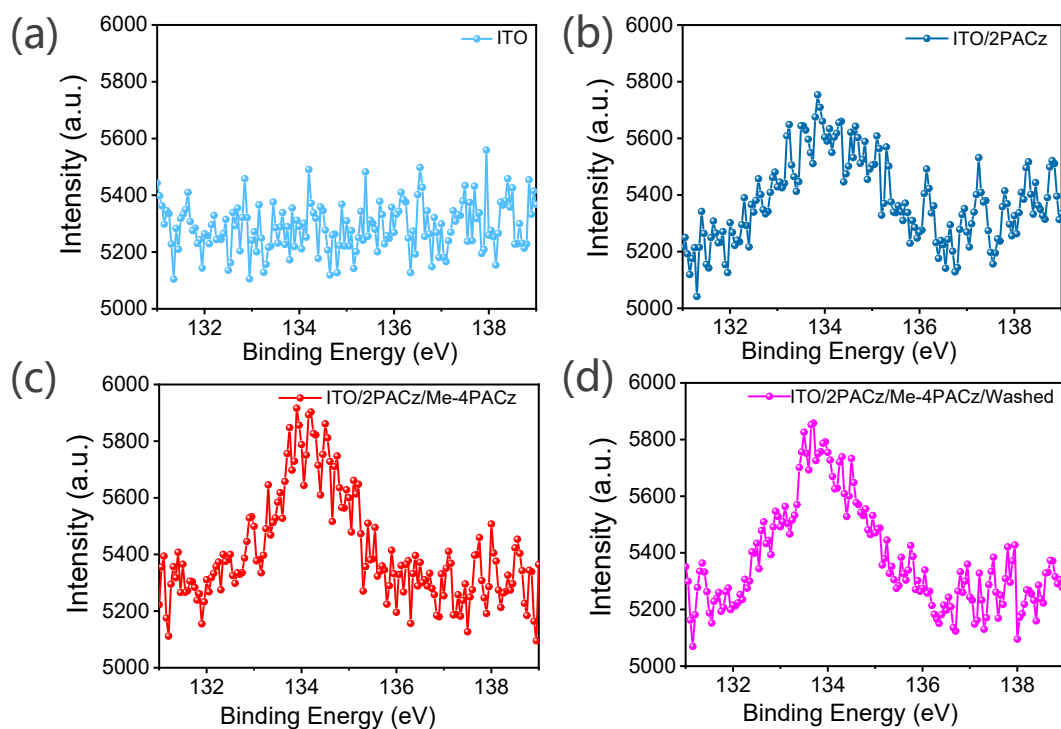
Figure S2. P 2p region of XPS spectra on ITO, ITO/2PACz, ITO/2PACz/Me-4PACz and solvent washed ITO/2PACz/Me-4PACz samples. Washing means the surface is dripped with abundant pure solvent (DMF: DMSO=4:1) and then spinning it immediately. We observed a significant increase in the phosphorus (P) content on the substrate after depositing the Me-4PACz layer and a slight decrease in the P content in the film after washing with pure DMF: DMSO solvent. These results ensure that the stacked small molecular layers are not totally washed away by subsequent perovskite solutions.
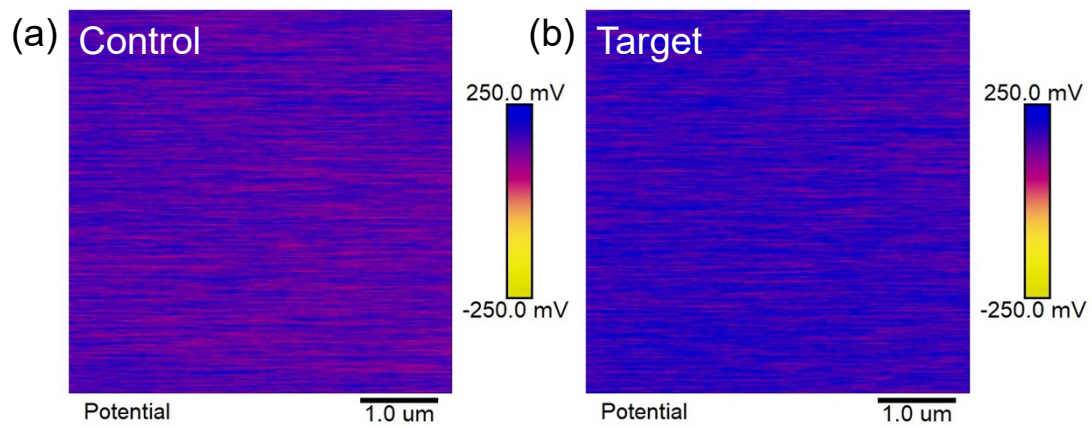
Figure S3. Surface potential distribution of different substrates (a) 2PACz and (b) 2PACz with Me-4PACz interface engineering.
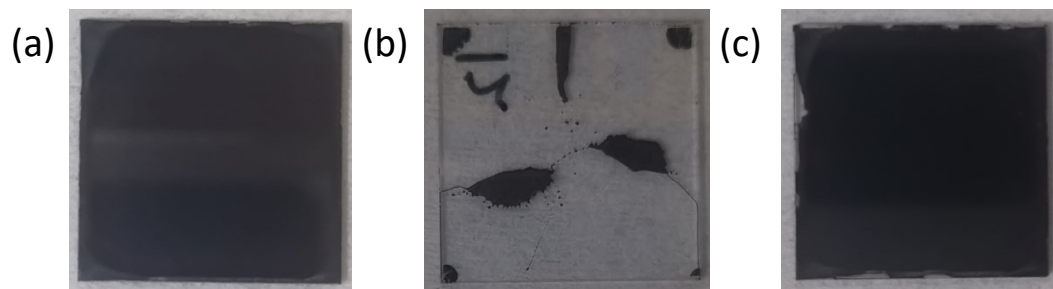
Figure S4. Optical images of perovskites deposited on different substrates (a) 2PACz, (b) Me-4PACz and (c) 2PACz with Me-4PACz interface engineering.

3.79Å

Binding Energy: 205 meV
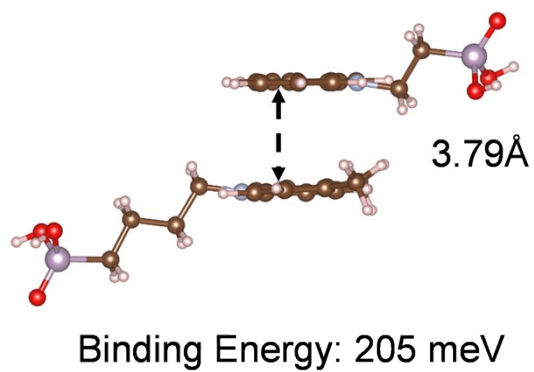
Figure S5. Schematic diagram represents corresponding dimers of Me-4PACz and 2PACz, and their stacking situation according to DFT calculations.
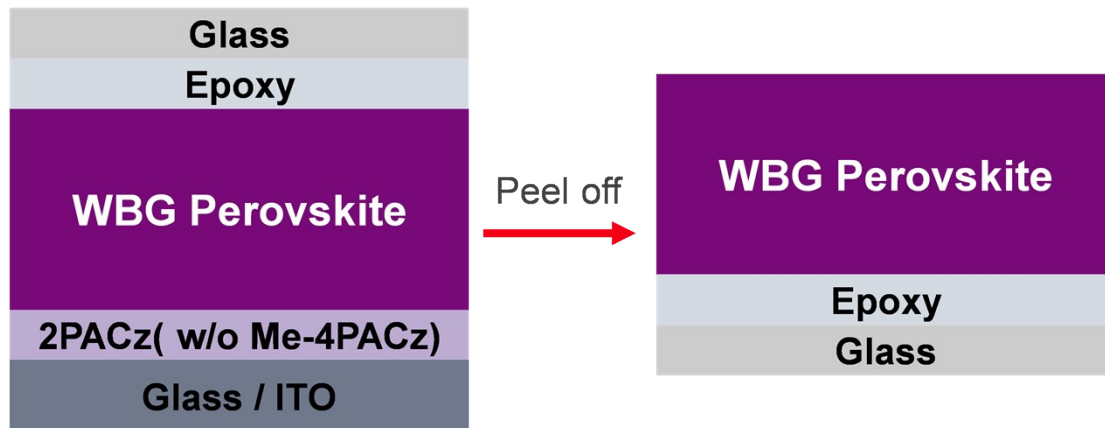
Figure S6. Schematic of peeling off perovskite films from ITO glass substrates with a two-component epoxy glue encapsulant. The buried interfaces are used for various characterization.
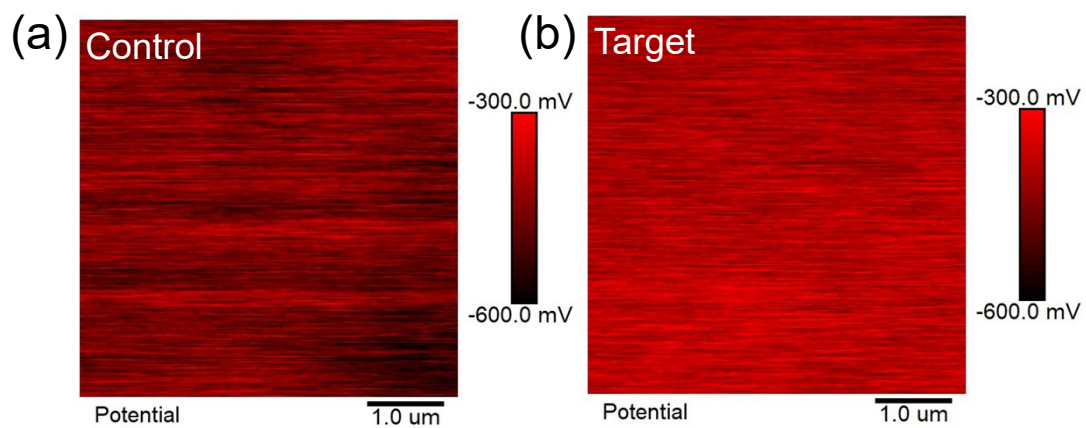
Figure S7. KPFM images of the control (a) and target (b) perovskite films at the perovskite burial interface.
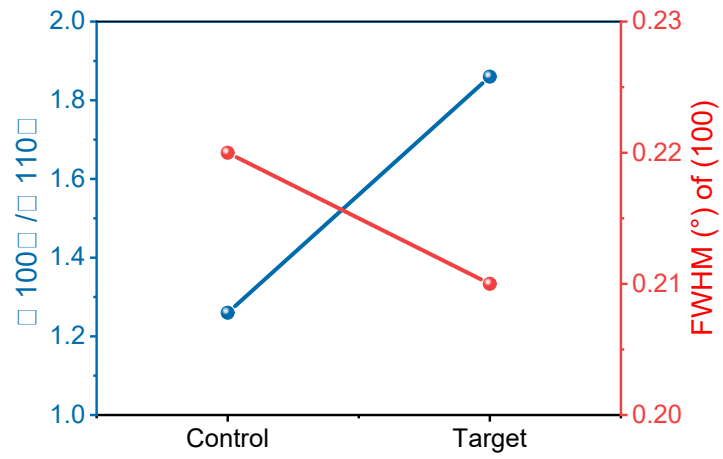
Figure S8. The FWHM of the (100) peak and the (100) / (110) intensity ratios of perovskite films on control and target substrates.
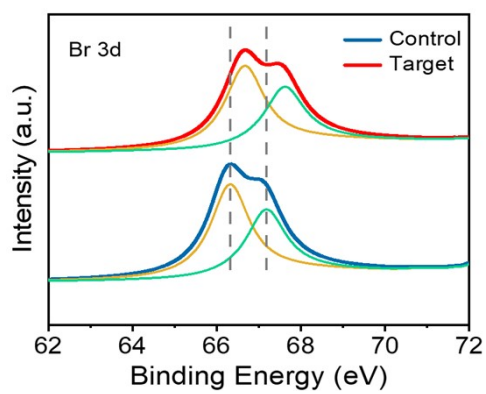
Figure S9. XPS spectra of Br 3d in the perovskite films with and without Me-4PACz interface engineering treatment.

(a) PbI$_2$ Me-4PACz

(b) PbI$_2$ DMSO

Binding Energy: -26.78 kcal mol^{-1} Binding Energy: -6.53 kcal mol^{-1}
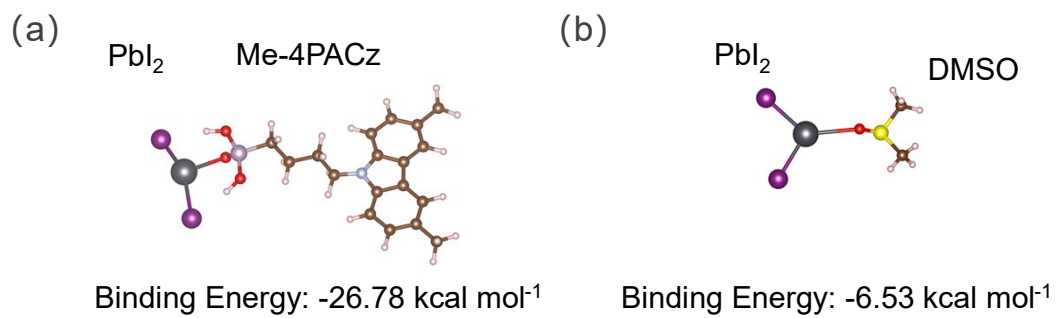
Figure S10. DFT calculation model for the coordination bonding interaction of Me-4PACz molecule (a) and DMSO molecule (b) with PbI$_2$ molecule, respectively.
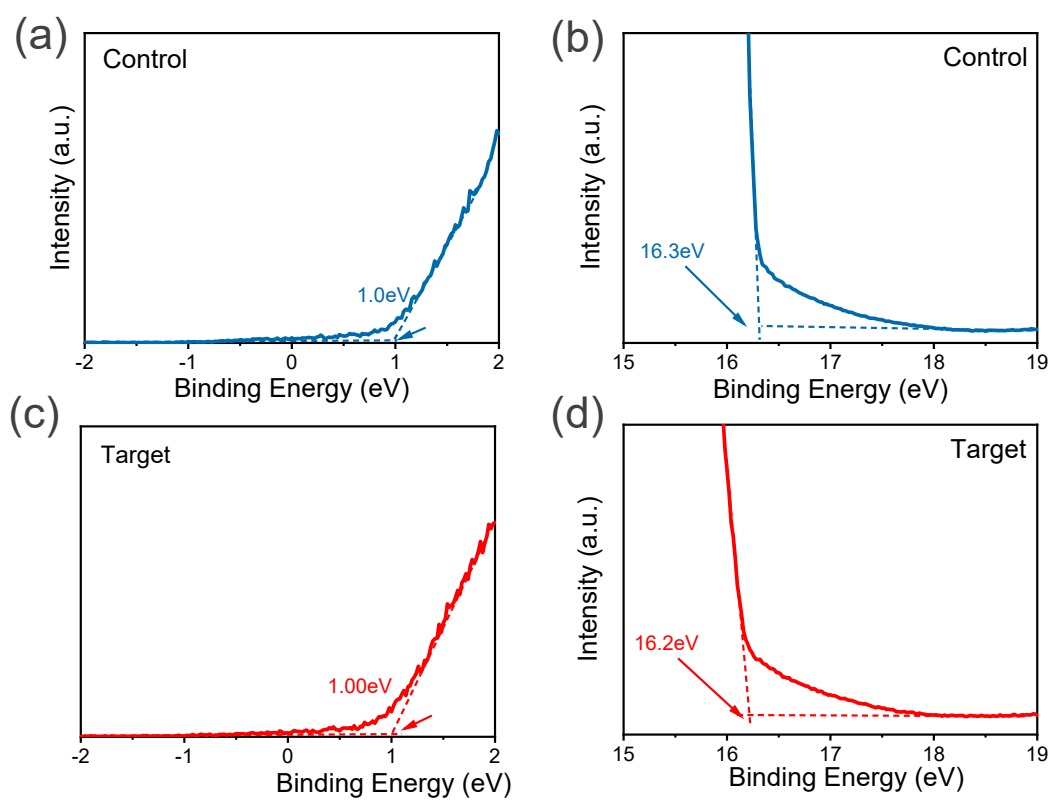
Figure S11. UPS spectra in the cutoff and the onset region for the perovskites (a) (b) without and (c) (d) with Me-4PACz interface engineering treatment.
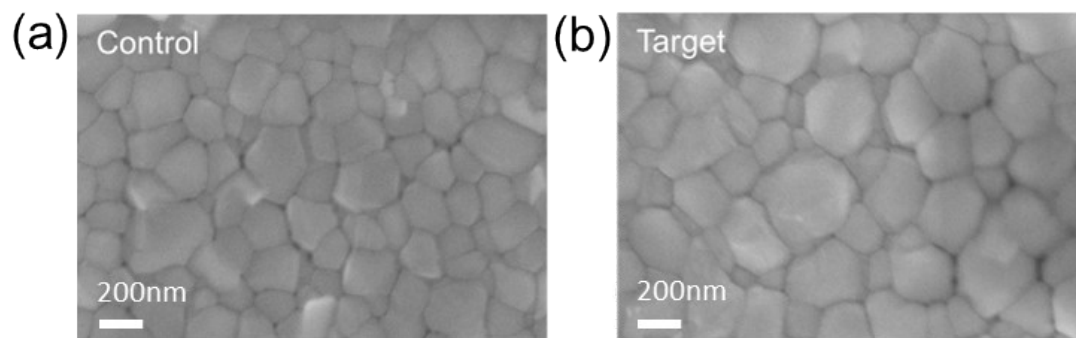
Figure S12. Top-view SEM images of perovskite thin films of control (a) and target (b) devices.
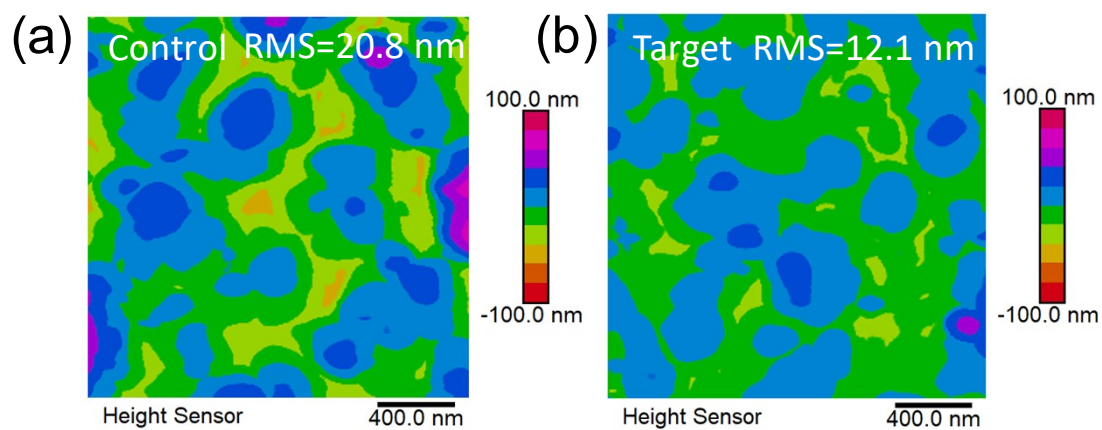
Figure S13. The surface AFM topographies of the perovskite films on the control (a) and the target (b) substrates. The color change represents the undulation of the height of the perovskite film surface, and the target device has less undulation than the control device.
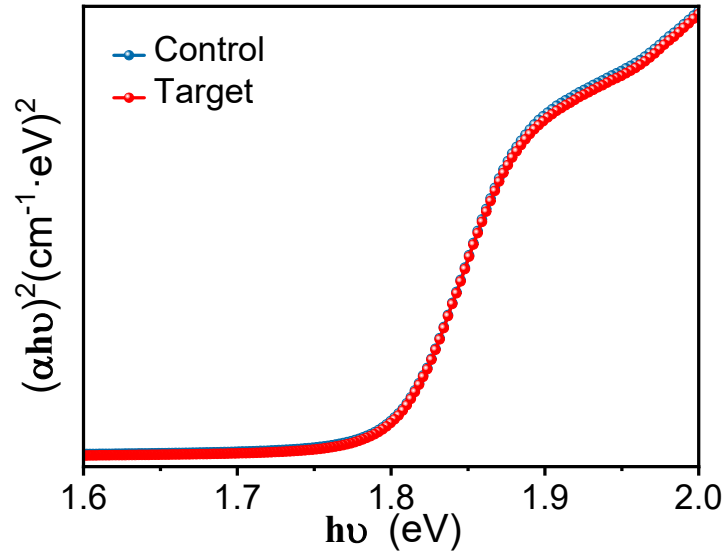
Figure S14. Taut plot of perovskite films deposited on different substrates. The results indicated that there were no significant changes observed in the absorption spectra between the different substrates.
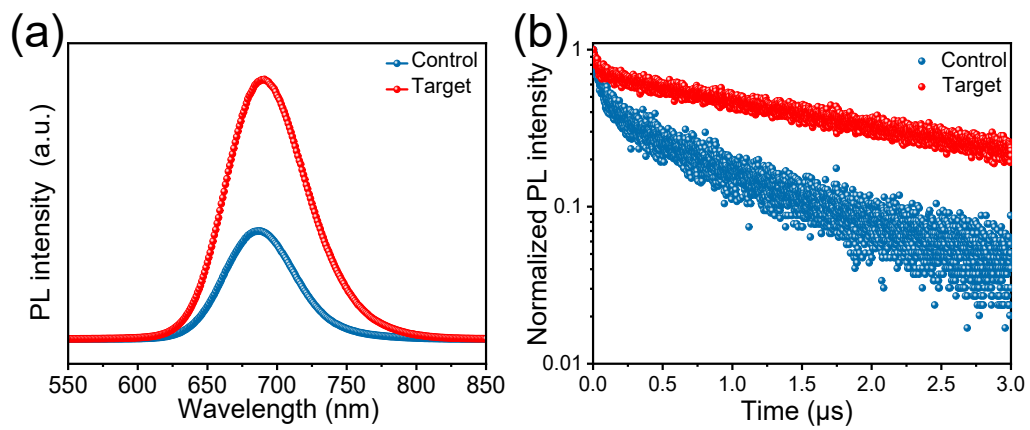
Figure S15. (a) PL and (b) TRPL spectra of perovskite films with and without Me-4PACz interface engineering treatment.
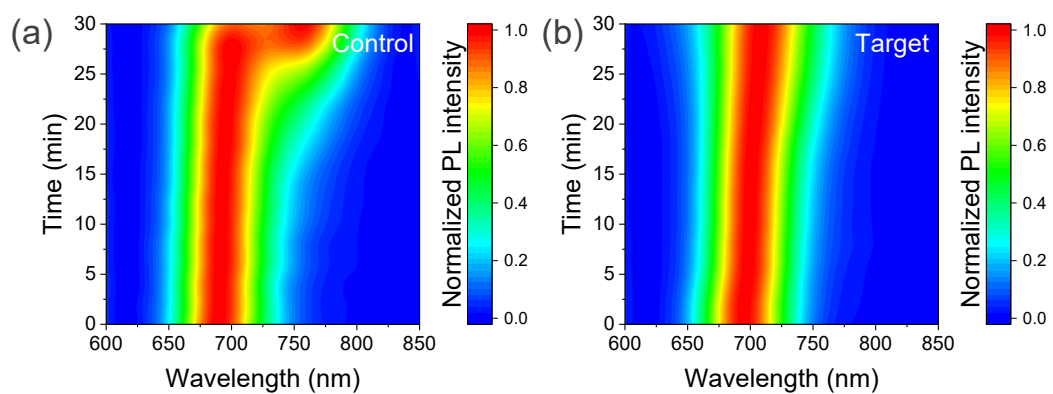
Figure S16. Normalized PL intensity spectra of perovskite films as a function of time duration under laser excitation without (a) and with (b) Me-4PACz interface engineering treatment.
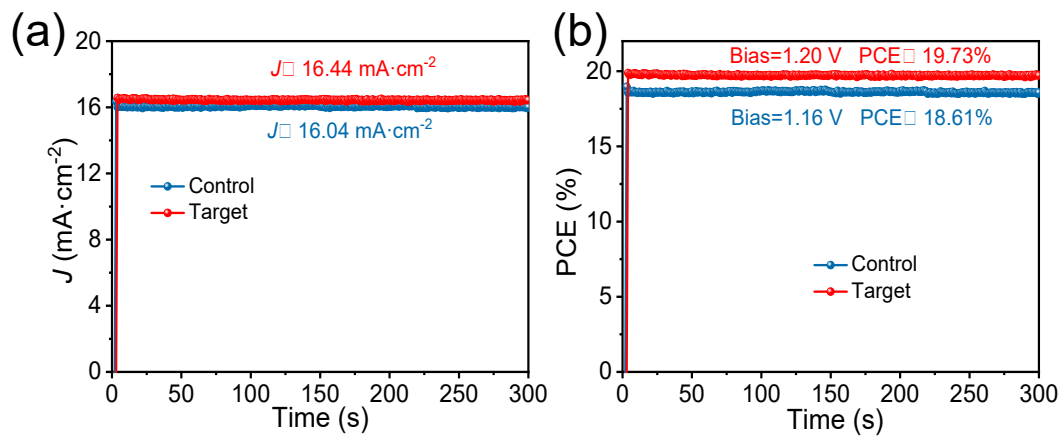
Figure S17. Stabilized power output of the devices with and without Me-4PACz interface engineering treatment biased at the maximum power point.
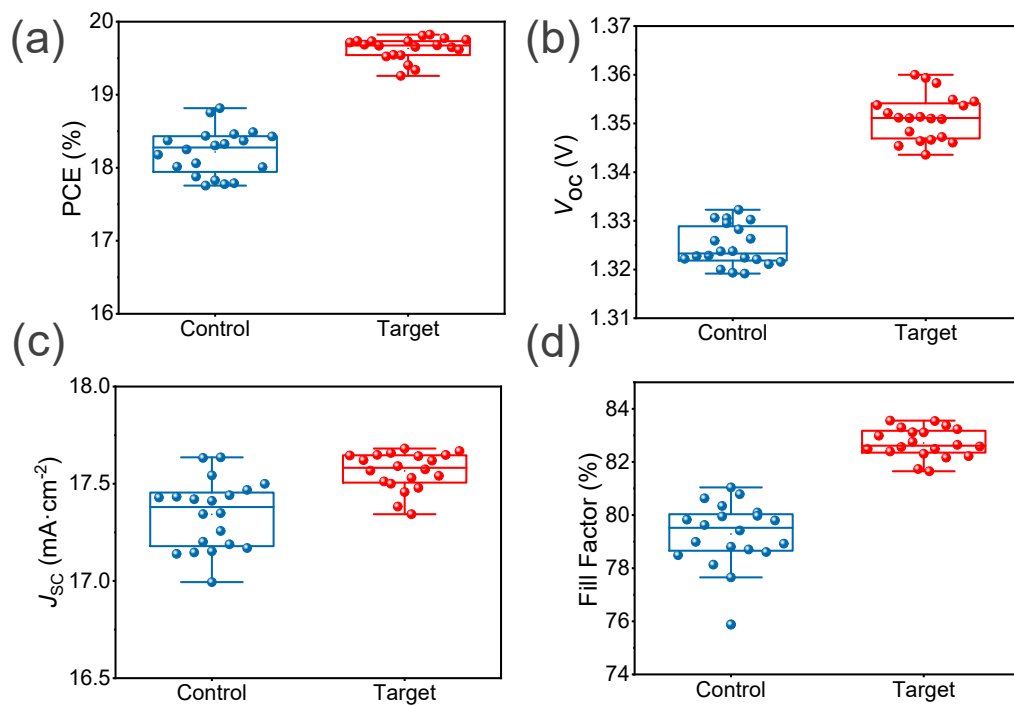
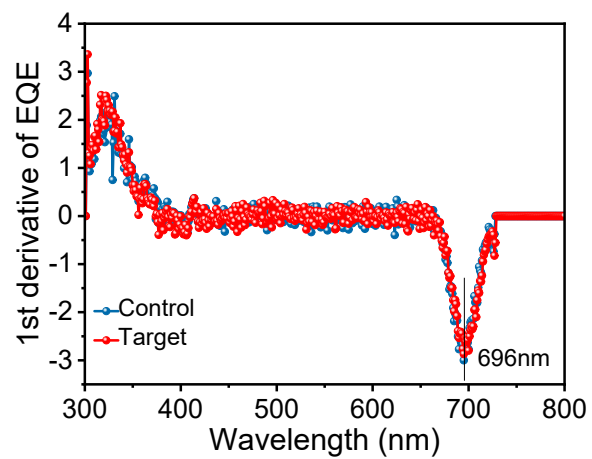**Figure S18.** The statistical distribution of device performance parameters PCE (a), V_{OC} (b), J_{SC} (c) and FF (d).

Figure S19. The corresponding EQE derivation calculation results for band gap values.
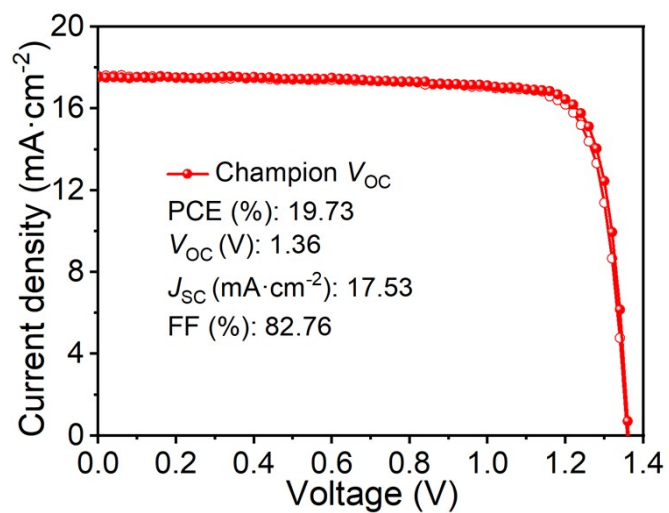
Figure S20. *J–V* curves of the champion V_{OC} device.

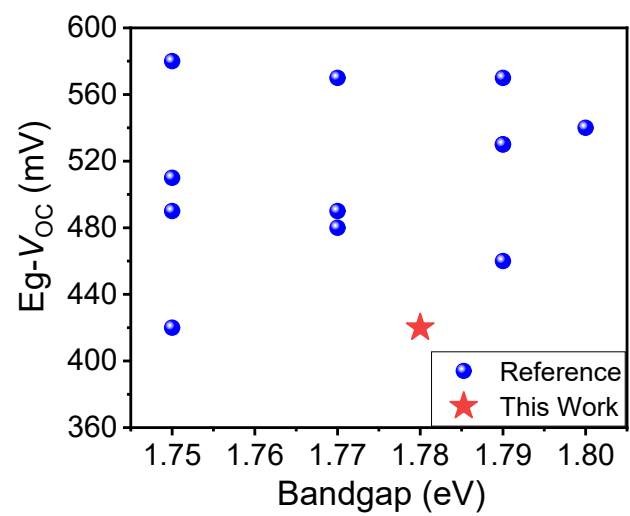**Figure S21.** V_{OC}-deficit values from literature reported for WBG (1.75~1.85 eV) perovskite solar cells.
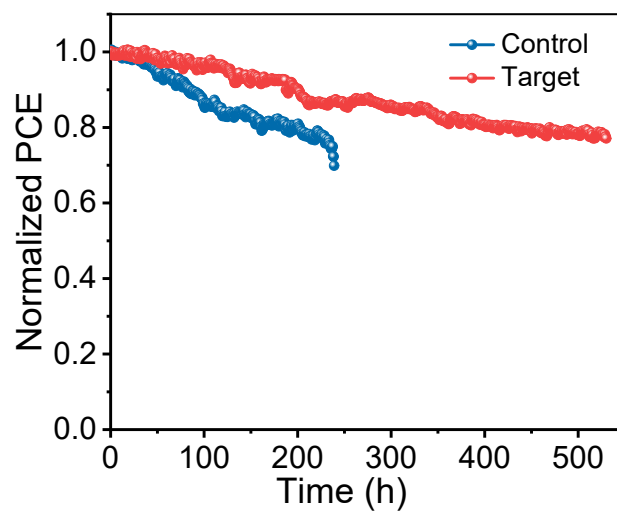
Figure S22. Maximum power point tracking (MPPT) of the devices with and without Me-4PACz interface engineering treatment in N_2 under 100 mW cm^{-2} white light illumination at 50 °C.
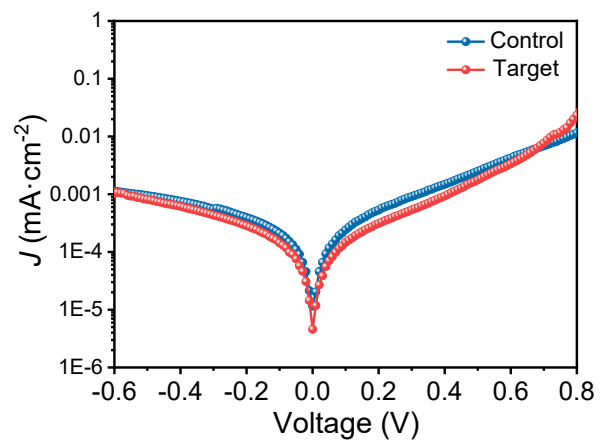
Figure S23. The dark current density-voltage (*J-V*) curves of the control and target devices.
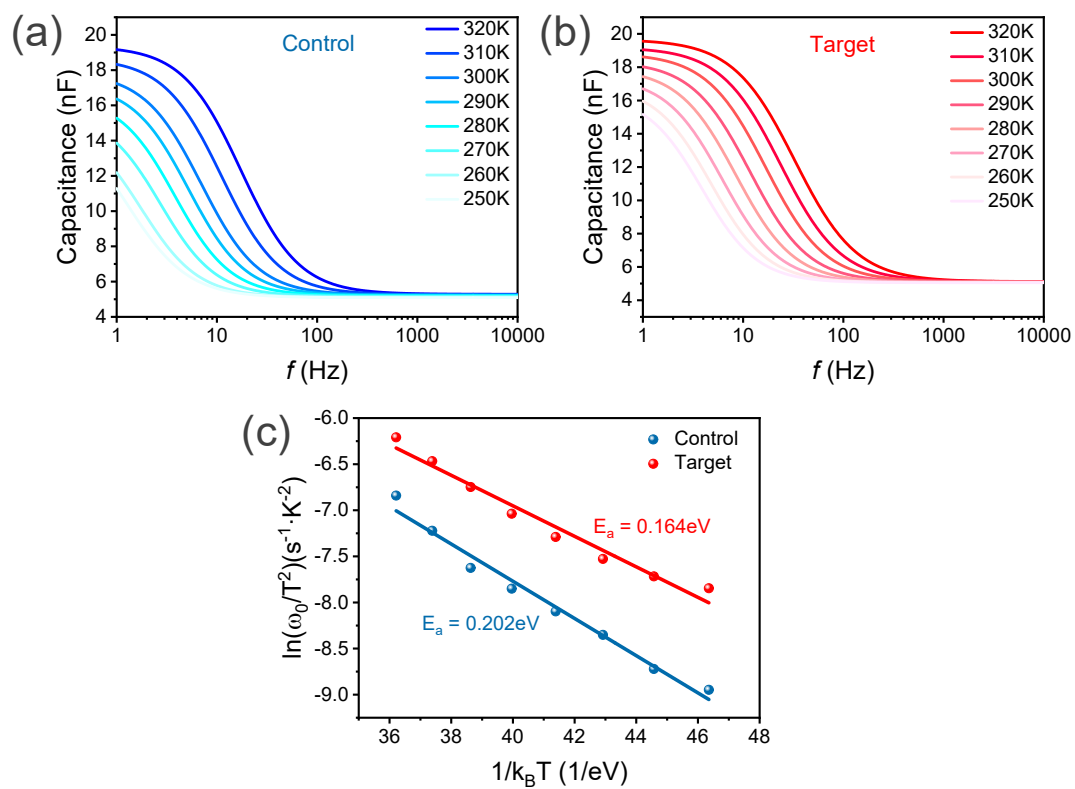
Figure S24. Admittance spectra of WBG PSCs (a) without and (b) with Me-4PACz interface engineering treatment and (c) the corresponding Arrhenius plot.
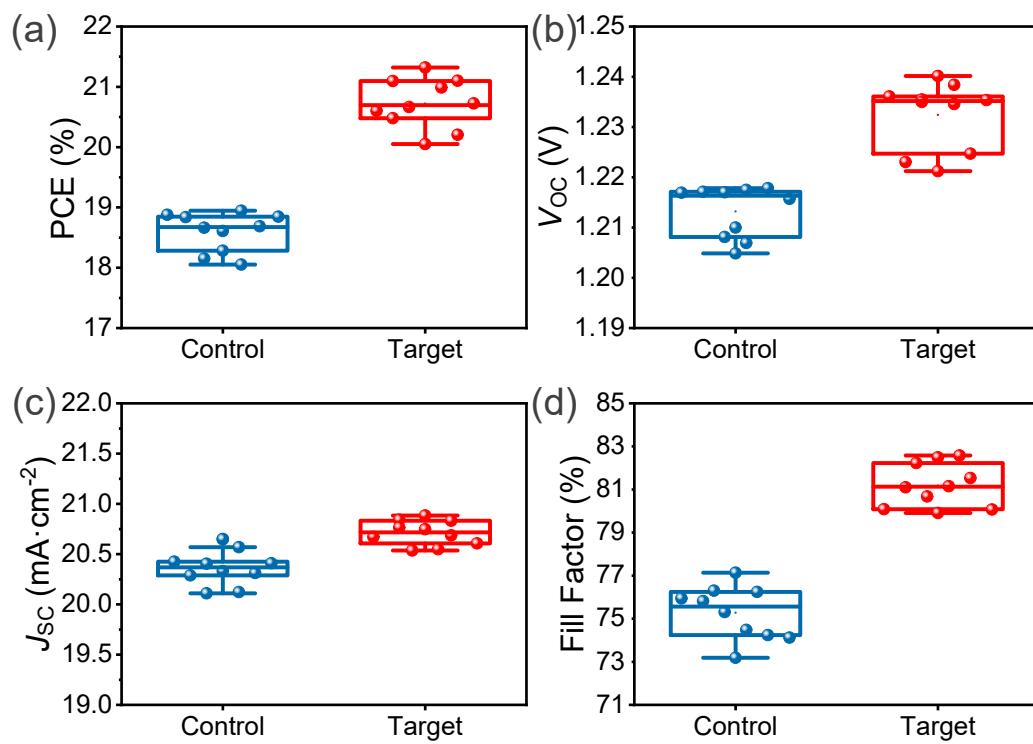
Figure S25. Statistical results of PCE (a)、V_{OC} (b)、J_{SC} (c) and FF (d) of 1.66 eV wide-Eg PSCs.
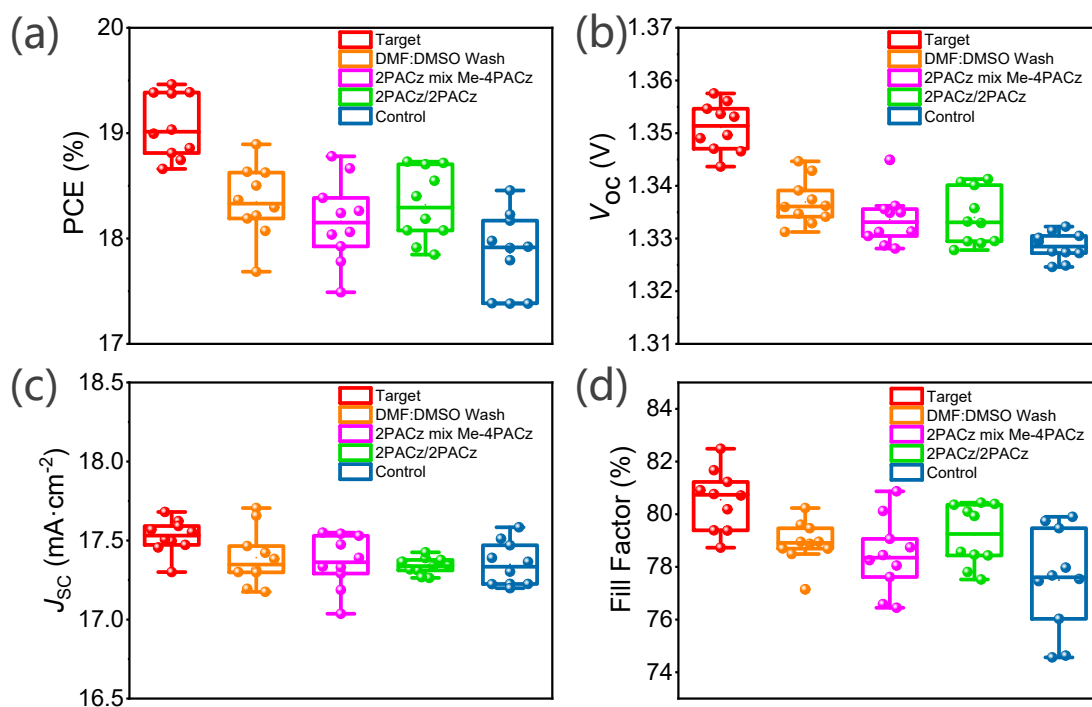
Figure S26. Statistical results of PCE (a)、V_{OC} (b)、J_{SC} (c) and FF (d) using different hole selective layers. 2PACz/2PACz represents sequential deposition of two layers of 2PACz. 2PACz mix Me-4PACz represents a mixture of 2PACz: Me-4PACz=4:1. DMF: DMSO Wash represents washing of the stacked small molecules on target substrate using a pure DMF: DMSO=4:1 solvent.
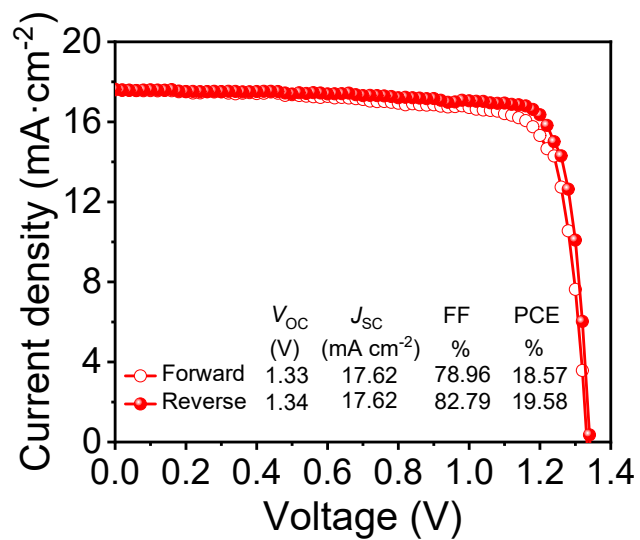
Figure S27. *J–V* curves of the champion device with stacked 2PACz and Me-4PACz using the blade coating method.
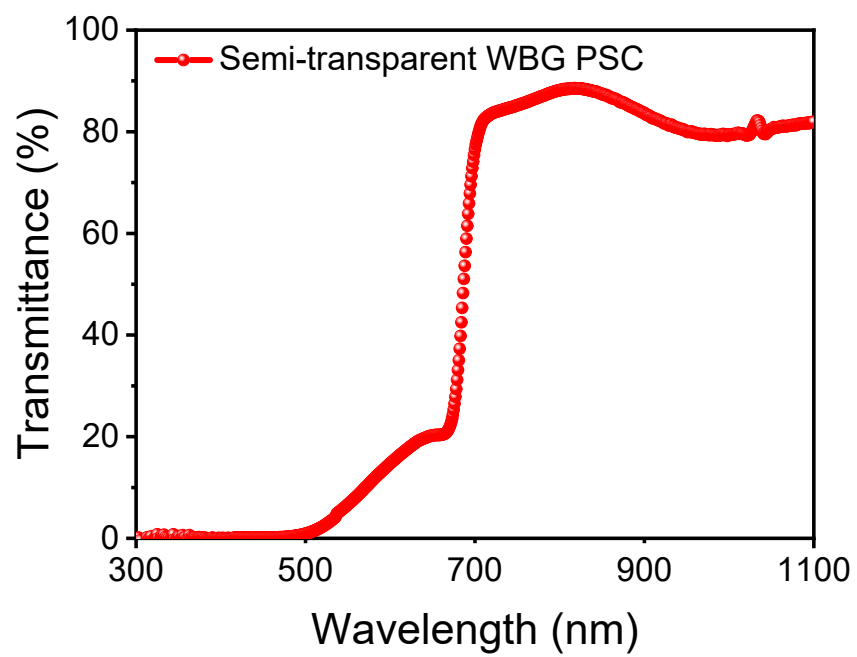
Figure S28. Transmission spectrum of a semi-transparent WBG PSC.

Table S1. Carrier lifetimes obtained from TRPL spectra of perovskite films with and without Me-4PACz interface engineering treatment.

Sample	τ_1(ns)	τ_2(ns)	average lifetime(ns)
Control	63	955	872
Target	39	2264	2257

Table S2. Photovoltaic performance of the literature reported organic-inorganic hybrid inverted WBG (1.75 ~ 1.85 eV) PSCs.

| Sample	Bandgap (eV)	V_{OC} (V)	Ref.
$FA_{0.8}Cs_{0.2}Pb(I_{0.7}Br_{0.3})_3$	1.75	1.24	[3]
$FA_{0.58}GA_{0.10}Cs_{0.32}Pb(I_{0.73}Br_{0.27})_3$	1.75	1.24	[4]
$(FA_{0.6}MA_{0.4})_{0.9}Cs_{0.1}Pb(I_{0.6}Br_{0.4})_3$	1.75	1.26	[5]
$Cs_{0.3}FA_{0.6}DMA_{0.1}Pb(I_{0.7}Br_{0.3})_3$	1.75	1.33	[6]
$FA_{0.8}Cs_{0.2}Pb(I_{0.6}Br_{0.4})_3$	1.77	1.20	[7]
$FA_{0.8}Cs_{0.2}Pb(I_{0.6}Br_{0.4})_3$	1.77	1.28	[8]
$FA_{0.8}Cs_{0.12}MA_{0.08}PbI_{1.8}Br_{1.2}$	1.77	1.29	[9]
$FA_{0.8}Cs_{0.2}Pb(I_{0.6}Br_{0.4})_3$	1.77	1.31	[10]
$FA_{0.83}Cs_{0.17}Pb(I_{0.6}Br_{0.4})_3$	1.79	1.22	[11]
$FA_{0.8}Cs_{0.2}Pb(I_{0.6}Br_{0.4})_3$	1.79	1.26	[12]
$FA_{0.75}Cs_{0.25}Pb(I_{0.6}Br_{0.4})_3$	1.79	1.26	[13]
$FA_{0.8}Cs_{0.2}Pb(I_{0.6}Br_{0.4})_3$	1.79	1.33	[14]
$DMA_{0.1}FA_{0.5}Cs_{0.4}MA_{0.05}Pb(I_{0.75}Br_{0.25})_3Cl_{0.15}$	1.80	1.26	[15]
$FA_{0.8}Cs_{0.2}Pb(I_{0.6}Br_{0.4})_3$	**1.78**	**1.36**	**This work**

Table S3. The series resistance (R_S) and recombination resistance (R_{rec}) obtained from electronic impedance spectroscopy (EIS) spectra of perovskite films with and without Me-4PACz interface engineering treatment.

Sample	$R_S(\Omega)$	$R_{rec}(\Omega)$
Control	9.3	364.3
Target	8.9	1253.4

Table S4. Summary of the state-of-the-art 4-T all-perovskite tandem solar cells (TSCs).

Year	V_{OC} (V) WBG/NBG	PCE (%)	Ref.
2017	1.14/0.81	21.00	[16]
2018	1.20/0.81	23.10	[1]
2019	1.12/0.81	25.00	[17]
2021	1.16/0.78	24.80	[18]
2022	1.15/0.83	26.01	[19]
2022	1.27/0.83	25.17	[20]
2023	1.15/0.82	26.30	[21]
2023	1.18/0.80	26.64	[22]
2023	1.26/0.86	26.24	[23]
2023	**1.32/0.86**	**28.05**	**This work**

Reference

1 D. Zhao, C. Wang, Z. Song, Y. Yu, C. Chen, X. Zhao, K. Zhu and Y. Yan, *ACS Energy Lett.*, 2018, **3**, 305–306.

2 P. Caprioglio, M. Stolterfoht, C. M. Wolff, T. Unold, B. Rech, S. Albrecht and D. Neher, *Adv. Energy Mater.*, 2019, **9**, 1901631.

3 C. Chen, Z. Song, C. Xiao, D. Zhao, N. Shrestha, C. Li, G. Yang, F. Yao, X. Zheng, R. J. Ellingson, C.-S. Jiang, M. Al-Jassim, K. Zhu, G. Fang and Y. Yan, *Nano Energy*, 2019, **61**, 141–147.

4 R. J. Stoddard, A. Rajagopal, R. L. Palmer, I. L. Braly, A. K.-Y. Jen and H. W. Hillhouse, *ACS Energy Lett.*, 2018, **3**, 1261–1268.

5 Z. Li, J. Zhang, S. Wu, X. Deng, F. Li, D. Liu, C. Lee, F. Lin, D. Lei, C.-C. Chueh, Z. Zhu and A. K.-Y. Jen, *Nano Energy*, 2020, **78**, 105377.

6 Q. Jiang, J. Tong, R. A. Scheidt, X. Wang, A. E. Louks, Y. Xian, R. Tirawat, A. F. Palmstrom, M. P. Hautzinger, S. P. Harvey, S. Johnston, L. T. Schelhas, B. W. Larson, E. L. Warren, M. C. Beard, J. J. Berry, Y. Yan and K. Zhu, *Science*, 2022, **378**, 1295–1300.

7 Y. Wang, S. Gu, G. Liu, L. Zhang, Z. Liu, R. Lin, K. Xiao, X. Luo, J. Shi, J. Du, F. Meng, L. Li, Z. Liu and H. Tan, *Sci. China Chem.*, 2021, **64**, 2025–2034.

8 R. He, Z. Yi, Y. Luo, J. Luo, Q. Wei, H. Lai, H. Huang, B. Zou, G. Cui, W. Wang, C. Xiao, S. Ren, C. Chen, C. Wang, G. Xing, F. Fu and D. Zhao, *Adv. Sci.*, 2022, **9**, 2203210.

9 H. Lai, J. Luo, Y. Zwirner, S. Olthof, A. Wieczorek, F. Ye, Q. Jeangros, X. Yin, F. Akhundova, T. Ma, R. He, R. K. Kothandaraman, X. Chin, E. Gilshtein, A. Müller, C. Wang, J. Thiesbrummel, S. Siol, J. M. Prieto, T. Unold, M. Stolterfoht, C. Chen, A. N. Tiwari, D. Zhao and F. Fu, *Adv. Energy Mater.*, 2022, **12**, 2202438.

10 J. Zhu, Y. Luo, R. He, C. Chen, Y. Wang, J. Luo, Z. Yi, J. Thiesbrummel, C. Wang, F. Lang, H. Lai, Y. Xu, J. Wang, Z. Zhang, W. Liang, G. Cui, S. Ren, X. Hao, H. Huang, Y. Wang, F. Yao, Q. Lin, L. Wu, J. Zhang, M. Stolterfoht, F. Fu and D. Zhao, *Nat. Energy*, , DOI:10.1038/s41560-023-01274-z.

11 R. D. J. Oliver, P. Caprioglio, F. Peña-Camargo, L. R. V. Buizza, F. Zu, A. J. Ramadan, S. G. Motti, S. Mahesh, M. M. McCarthy, J. H. Warby, Y.-H. Lin, N. Koch, S. Albrecht, L. M. Herz, M. B. Johnston, D. Neher, M. Stolterfoht and H. J. Snaith, *Energy Environ. Sci.*, 2022, **15**, 714–726.

12 C. Wang, W. Shao, J. Liang, C. Chen, X. Hu, H. Cui, C. Liu, G. Fang and C. Tao, *Small*, 2022, **18**, 2204081.

13 W. Chen, Y. Zhu, J. Xiu, G. Chen, H. Liang, S. Liu, H. Xue, E. Birgersson, J. W. Ho, X. Qin, J. Lin, R. Ma, T. Liu, Y. He, A. M.-C. Ng, X. Guo, Z. He, H. Yan, A. B. Djurišić and Y. Hou, *Nat. Energy*, 2022, **7**, 229–237.

14 H. Chen, A. Maxwell, C. Li, S. Teale, B. Chen, T. Zhu, E. Ugur, G. Harrison, L. Grater, J. Wang, Z. Wang, L. Zeng, S. M. Park, L. Chen, P. Serles, R. A. Awni, B. Subedi, X. Zheng, C. Xiao, N. J. Podraza, T. Filleter, C. Liu, Y. Yang, J. M. Luther, S. De Wolf, M. G. Kanatzidis, Y. Yan and E. H. Sargent, *Nature*, 2023, **613**, 676–681.

15 J. Wen, Y. Zhao, Z. Liu, H. Gao, R. Lin, S. Wan, C. Ji, K. Xiao, Y. Gao, Y. Tian, J. Xie, C. J. Brabec and H. Tan, *Adv. Mater.*, 2022, **34**, 2110356.

16 D. Zhao, Y. Yu, C. Wang, W. Liao, N. Shrestha, C. R. Grice, A. J. Cimaroli, L. Guan, R. J. Ellingson, K. Zhu, X. Zhao, R.-G. Xiong and Y. Yan, *Nat. Energy*, 2017, **2**, 17018.

17 J. Tong, Z. Song, D. H. Kim, X. Chen, C. Chen, A. F. Palmstrom, P. F. Ndione, M. O. Reese, S. P. Dunfield, O. G. Reid, J. Liu, F. Zhang, S. P. Harvey, Z. Li, S. T. Christensen, G. Teeter, D. Zhao, M. M. Al-Jassim, M. F. A. M. Van Hest, M. C. Beard, S. E. Shaheen, J. J. Berry, Y. Yan and K. Zhu, *Science*, 2019, **364**, 475–479.

18 H. Hu, S. Moghadamzadeh, R. Azmi, Y. Li, M. Kaiser, J. C. Fischer, Q. Jin, J. Maibach, I. M. Hossain, U. W. Paetzold and B. Abdollahi Nejand, *Adv. Funct. Mater.*, 2022, **32**, 2107650.

19 W. Zhang, L. Huang, W. Zheng, S. Zhou, X. Hu, J. Zhou, J. Li, J. Liang, W. Ke and G. Fang, *Nano Energy*, 2022, **96**, 107078.

20 R. He, Z. Yi, Y. Luo, J. Luo, Q. Wei, H. Lai, H. Huang, B. Zou, G. Cui, W. Wang, C. Xiao, S. Ren, C. Chen, C. Wang, G. Xing, F. Fu and D. Zhao, *Adv. Sci.*, 2022, **9**, 2203210.

21 X. Hu, J. Li, C. Wang, H. Cui, Y. Liu, S. Zhou, H. Guan, W. Ke, C. Tao and G. Fang, *Nano-Micro Lett.*, 2023, **15**, 103.

22 H. Guan, W. Zhang, J. Liang, C. Wang, X. Hu, D. Pu, L. Huang, Y. Ge, H. Cui, Y. Zou, G. Fang and W. Ke, *Adv. Funct. Mater.*, 2023, 2300860.

23 W. Wang, X. Liu, J. Wang, C. Chen, J. Yu, D. Zhao and W. Tang, *Adv. Energy Mater.*, 2023, 2300694.